Journal Name

ARTICLE TYPE

Cite this: DOI: 10.1039/xxxxxxxxxx

How cracks are hot and cool - a burning issue for paper – supplementary material†

Renaud Toussaint,*[a,b] Olivier Lengliné,[a,b] Stéphane Santucci,[c,b] Tom Vincent-Dospital,[a] Muriel Naert-Guillot,[a] and Knut Jørgen Måløy[d,b]

1 Computation of the Green kernel of diffusion with lateral losses

The Green function sought for, $G_1(x,y,t)$, is the solution of

$$\partial_t G_1(x,y,t) = D\nabla^2 G_1 - G_1/\tau + \delta(x)\delta(y)\delta(t) \tag{1}$$

with boundary conditions $G_1 \to 0$ when $x^2+y^2 \to \infty$ and initial conditions $G_1 = 0$ when $t < 0$.

Call G_0 the Green function of the classical two dimensional diffusion problem, without any extra loss term, i.e. the solution of

$$\partial_t G_0(x,y,t) = D\nabla^2 G_0(x,y,t) + \delta(x)\delta(y)\delta(t) \tag{2}$$

This Green function can be expressed as[1],

$$G_0(x,y,t) = \frac{1}{4\pi Dt} \exp\left[-\frac{x^2+y^2}{4Dt}\right] \tag{3}$$

Then, forming $G_0(x,y,t)e^{-t/\tau}$, we can check directly that

$$\begin{aligned} \partial_t(G_0(x,y,t)e^{-t/\tau}) &= \\ &\partial_t(G_0(x,y,t))e^{-t/\tau} - (G_0(x,y,t)e^{-t/\tau})/\tau \\ =\ & D\nabla^2 G_0(x,y,t) + \delta(x)\delta(y)\delta(t) - (G_0(x,y,t)e^{-t/\tau})/\tau \end{aligned} \tag{4}$$

and satisfies the proper intial and boundary conditions, i.e. the Green function sought for is $G_1(x,y,t) = G_0(x,y,t)e^{-t/\tau}$

Using the linearity of the problem, the solution of

$$\partial_t \Delta T(x,y,t) = D\nabla^2 \Delta T - \Delta T/\tau + g(x,y,t) \tag{5}$$

can be obtained by convolving the source $g(x,y,t)$ with the Green function $G_1(x,y,t)$, i.e. the solution is

$$\Delta T(x,y) = \int_0^t ds \int\int d\xi d\eta G_1(x-\xi, y-\eta, t-s) g(\xi,\eta,s) \tag{6}$$

which corresponds to the form used.

2 Calibration experiments

Two characteristics of the paper are independently obtained during two types of calibration experiments, detailed in the supplementary material: the inplane heat diffusion coefficient is determined by heating a localized zone in the paper, and determining the spread of the temperature rise by the second moment of the temperature elevation field. From the classical expression of heat diffusion, neglecting out of plane diffusion for short times, one expects to observe a temperature rise proportional to the Green function of diffusion, Eq. (3).

The standard deviation of a temperature profile through the center can be expressed, and should thus be:

$$\sigma = \sqrt{\int x^2 G_0(x,0,t)dx / \int G_0(x,0,t)dx} = \sqrt{4Dt} \tag{7}$$

Indeed, such behavior is observed for early times, as shows Fig. 1. This allows to determine an inplane heat diffusion constant around $D = 4.4 \cdot 10^{-8} m^2/s$.

Conversely, the out-of-plane thermal flux leads to a thermal decay rate due to loss into the surrounding air, formulated as $(T - T_{air})/\tau$. Heating paper sample homogeneously, and observing their temperature converge to the atmospheric one, allows to determine $\tau \simeq 5s$ - from Fig. 2.

3 Illustration of the far-field and crack tip temperature as function of the process zone size

Although the far field temperature increase at distances larger than the process zone size does not depend on this size, the maximum temperature around the crack tip is crucially dependent on this term. To illustrate this, Fig. 3 shows the temperature along the trajectory of the center of the process zone, for zones of sizes 100, 50, 20 and 10μm, at $v = 1$ cm/s, with the other parameters determines from the experimentsl($v = 1$ cm/s, $\alpha G/(\rho c) = 0.0025$ K m).

[a] Institut de Physique du Globe de Strasbourg, CNRS, EOST-University of Strasbourg, 5 rue Descartes, 67084 Strasbourg Cedex, France. Fax: +33 3 68 85 01 25; Tel: +33 3 68 85 03 37; E-mail: renaud.toussaint@unistra.fr
[b] Centre for Advanced Study at The Norwegian Academy of Science and Letters, Drammensveien 78, 0271 N-Oslo, Norway.
[c] University of Lyon, ENS de Lyon, University Claude Bernard, CNRS, Laboratoire de Physique, F-69342 Lyon, France.
[d] Department of Physics, University of Oslo, PB 1048 Blindern, NO-0316 Oslo, Norway.
† Electronic Supplementary Information (ESI) available: [details of any supplementary information available should be included here]. See DOI: 10.1039/b000000x/

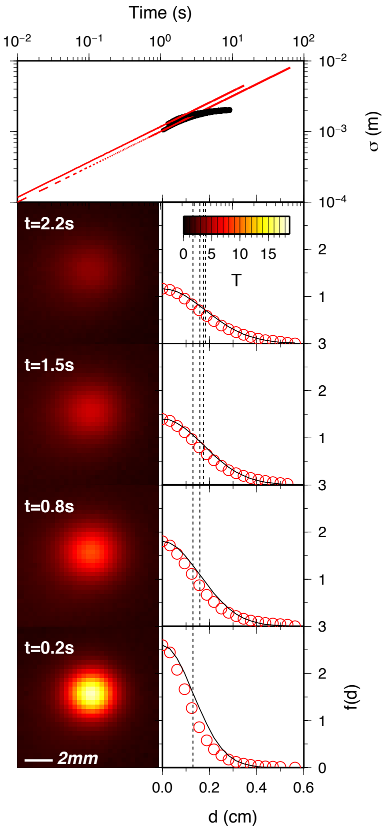

Fig. 1 Calibration experiments: Left: Measured temperature elevation T (in K), during the relaxation of a local heating. Right: Temperature elevation profiles across the hot spot during this relaxation, at distance d from the spot, with a spatial normalization: $f(d) = T(d)/\int T dS)$. The black curve represents a Gaussian fit. Top: Width σ of the Gaussian fits determined, as function of time, in bilogarithmic representation. The linear fits correspond to the predicted behavior $\sigma = \sqrt{4Dt}$ for in plane heat diffusion 2, and allow to determine D using the central value of the prefactor. The deviation at large times correspond to out of plane diffusion, that leads to a modified Green function G_1 where the tail of the distribution is screened.

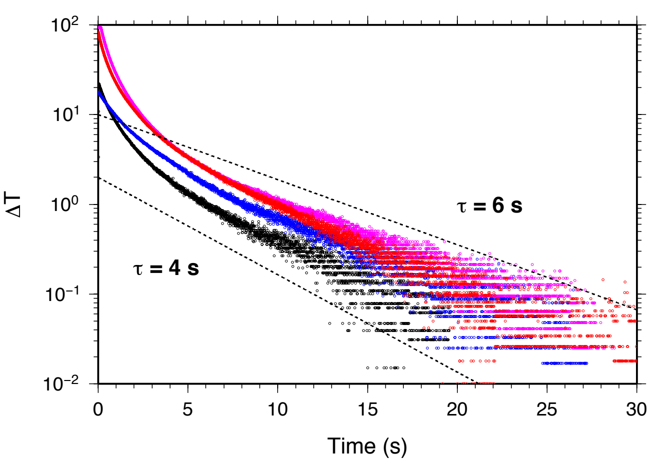

Fig. 2 Calibration experiments: Measured temperature (in K) during the relaxation of a global heating, in semilogarithmic representation, in three calibration experiments on three different paper samples. The relaxation according to a straight line corresponds to the predicted $\Delta T = \Delta T_0 e^{-t/\tau}$, the central slope allows to estimate τ.

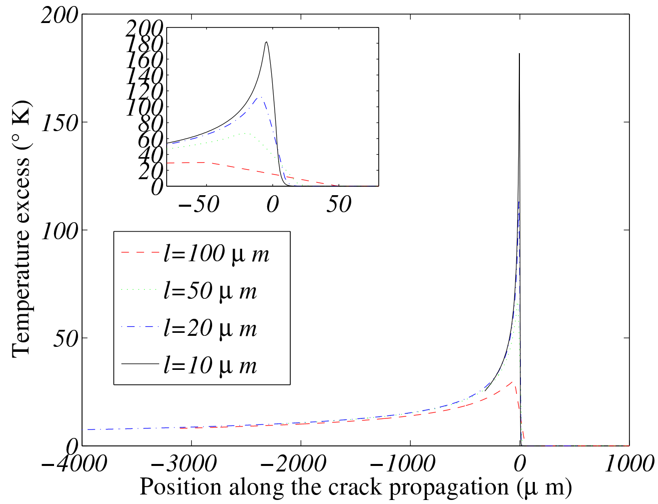

Fig. 3 Simulated temperature rise along the trajectory of the crack tip, for four different process zone sizes, $l = 20\mu$m (continuous), 50μm (dash-dotted) and 100μm (dashed curve), at similar crack velocities $v = 1$ cm/s. The far field temperatures are identical, and the maximum temperature rise reached ΔT, around the back of the process zone, varies importantly with the size of the process zone l - see zoom in the inset – according to the prediction, $\Delta T \simeq \alpha G/(\rho c l)$.

The far field temperature is identical in all cases, but the tip temperature is highly dependent on the process zone size – as seen in the inlet of Fig. 3 over a zone of 100μm. This is also visible in the temperature field map resulting from these simulations, and displayed at "large scale" (a few mm) in Fig. 4, for process zones of sizes $l = 20\mu$m , 50μm and 100μm, and at small scale (comparable to the process zone size) in Fig. 5 for a size of $l = 10\mu$m and Fig. 6 for $l = 20\mu$m , 50μm and 100μm.

The temperature reached in this case corresponds to an almost linear increase of temperature across the process zone from the front to the back, i.e. to a regime where the heat diffusion skindepth δ is smaller than the process zone size l, as seen on these zooms, and on the inset of Fig. 3 (see on the inset the straight temperature profiles from the head of the process zone, on the right, to the back of the process zone, on the left – these process zones are propagating to the right. The position of the head and back are at positions $\pm l/2$ in this representations, where l is the process zone size, 4 different curves with 4 different l values are displayed).

Simulations are also done for $v = 1mm/s$, with temperature along the tip trajectory shown in Fig. 7, and temperature rise fields shown in Fig. 8, for process zone sizes $l = 10, 20, 50, 100\mu$m.

Simulations are also done at $v = 0.1mm/s$, in the slow regime where $\delta > l$ for all process zone sizes probed, $l = 10, 20, 50, 100\mu$m. The temperature along the tip trajectory shown in Fig. 9, and temperature rise fields shown in Fig. 10, for process zone sizes $l = 10, 20, 50, 100\mu$m.

Eventually, simulations for a fast moving crack, $v = 1cm/s$, where done, the temperature rise along the tip trajectory is shown in Fig. 11.

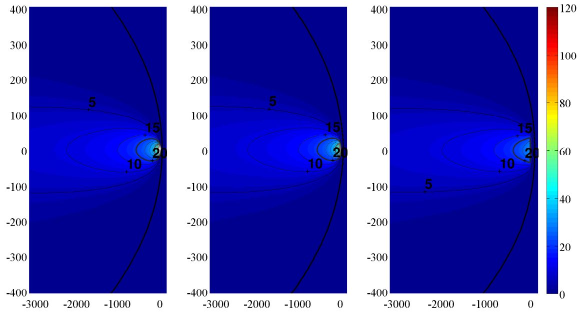

Fig. 4 Simulated temperature rise above the background one, around a crack tip moving at $v = 1$ cm/s, with a process zone of size (from left to right), $l = 20, 50, 100\mu$m , i.e. $10, 25, 50\mu$m radius. The color bar is in Kelvins, the spatial scale in μm.

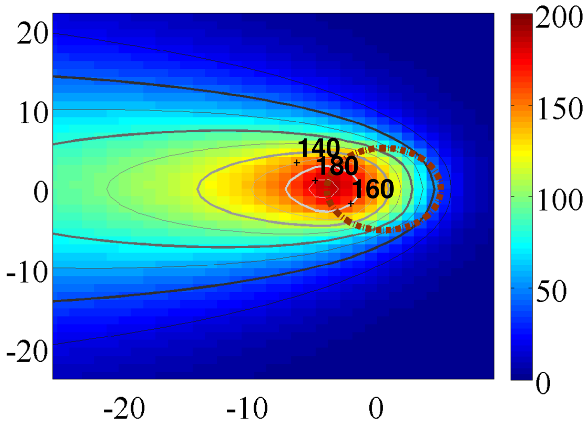

Fig. 5 Closeup view of the temperature rise above ambient temperature around the process zone, $v = 1$ cm/s, $l = 10\mu$m.The dash-dotted line indicates the limit of the process zone. The back of the process zone (left part, the crack moving to the right) could reach a temperature where oxidization of cellulose takes place over a micrometric zone. The color bar is in Kelvins, the spatial scale in μm.

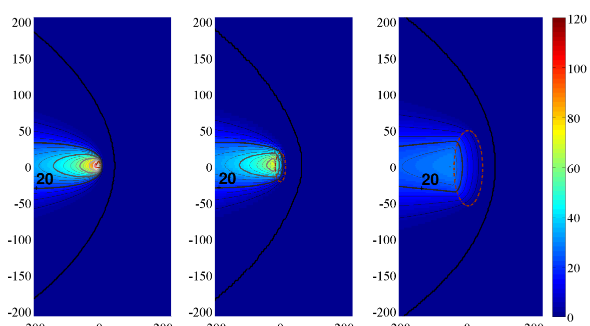

Fig. 6 Closeup view of the temperature rise around the process zone, $v = 1$ cm/s, , with different process zone sizes: from left to right, $l = 20, 50, 100\mu$m. The color bar is in Kelvins, the spatial scale in μm.

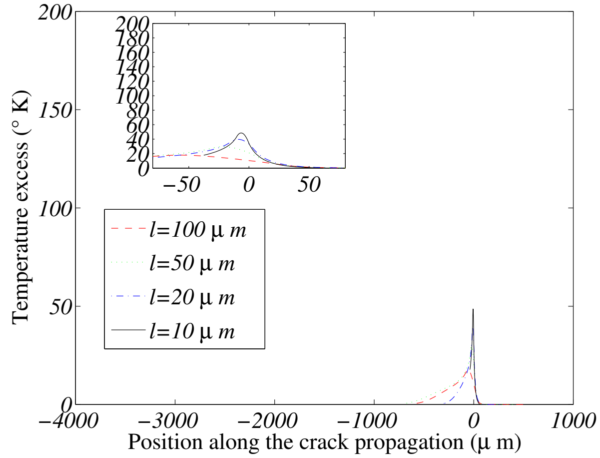

Fig. 7 Temperature rise across the trajectory of the crack tip, propagation velocity $v = 1$ mm/s.

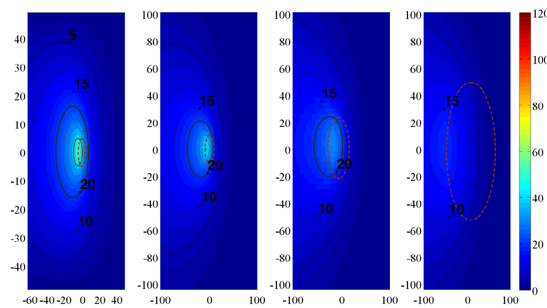

Fig. 8 Closeup view of the temperature rise around the process zone, $v = 1$ mm/s, with different process zone sizes: from left to right, $l = 10, 20, 50, 100\mu$m. The color bar is in Kelvins, the spatial scale in μm.

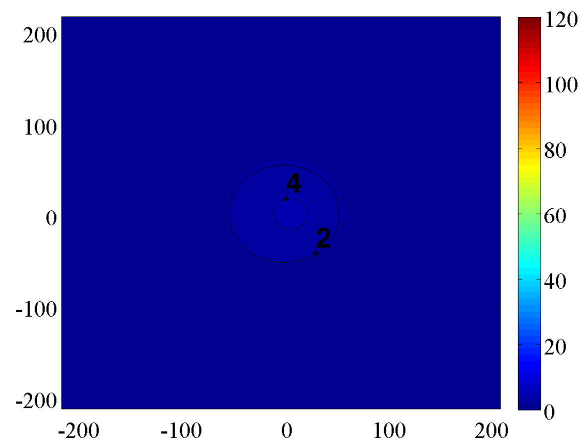

Fig. 9 Temperature rise across the trajectory of the crack tip, propagation velocity $v = 0.1$ mm/s, $l = 10\mu$m. The temperature scale is in Kelvins, the spatial scale in μm.

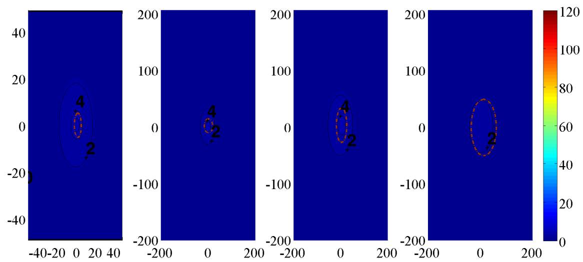

Fig. 10 Closeup view of the temperature rise around the process zone, $v = 0.1$ mm/s, $l = 10, 20, 50, 100\mu$m. The temperature scale is in Kelvins, the spatial scale in μm.

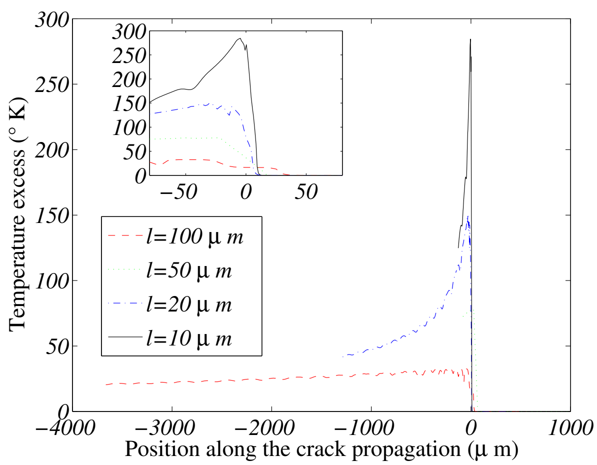

Fig. 11 Temperature rise across the trajectory of the crack tip, propagation velocity $v = 10$ cm/s, $l = 10, 20, 50, 100\mu$m.

4 Numerical resolution of heat transport and generation via the Alternating Direction Implicit Method.

The partial differential equation to solve, Eq. (1) in the main text, is:

$$\partial_t \Delta T = D\nabla^2 \Delta T - \Delta T/\tau + \alpha G f(x,y,t) h\nu/(\rho c), \qquad (8)$$

where $f(x,y,t)h$ is a normalized constant, equal to $4/(\pi l^2)$ over a disk of diameter l centered on the crack tip, modeled as moving at constant speed.

The initial state is a uniform null temperature excess over the room one, $\Delta T = 0$.

The resolution is made using the Alternating Direction Implicit Method, a variant of the Cranck-Nicholson one, which guarantees inconditional stability[2].

Writing $\Delta T(x_i, y_j, t_n) = u^n_{i,j}$ on a discrete square lattice of step Δx with time steps of size Δt, so that $x_i = x_0 + i\Delta x, y_j = y_0 + j\Delta x, t_n = t_0 + n\Delta t$, the discretized time step is split in two half steps, with alternatively an implicit expression of the Laplacian operator over x and an explicit one over y, or the contrary: this corresponds to

$$\begin{aligned}
\frac{u^{n+1/2}_{i,j} - u^n_{i,j}}{\Delta t/2} &= D(\delta^2_x u^{n+1/2}_{i,j} + \delta^2_y u^n_{i,j}) - \frac{u^n_{i,j}}{\tau} + \Omega^n_{i,j} \qquad (9)\\
\frac{u^{n+1}_{i,j} - u^{n+1/2}_{i,j}}{\Delta t/2} &= D(\delta^2_x u^{n+1/2}_{i,j} + \delta^2_y u^{n+1}_{i,j}) - \frac{u^{n+1/2}_{i,j}}{\tau} + \Omega^{n+1/2}_{i,j}
\end{aligned}$$

where the source term is $\Omega^n_{i,j} = \alpha G f(x_i, y_j, t_n) h\nu/(\rho c)$ and the second order spatial derivative operators on a field Φ are written

$$\begin{aligned}
\delta^2_x \Phi_{i,j} &= \Phi_{i-1,j} - 2\Phi_{i,j} + \Phi_{i+1,j}\\
\delta^2_y \Phi_{i,j} &= \Phi_{i,j-1} - 2\Phi_{i,j} + \Phi_{i,j-1} \qquad (10)
\end{aligned}$$

The boundary conditions, in the far field, correspond to $u = 0$ on the boundary nodes. To avoid influence of the boundary condition, the simulations are carried out with boundaries further away than two times the diffusion skindepth, $4\sqrt{D(t-t_0)}$ from the trajectory of the crack tip. The crack, center of the process zone, is displaced by $v\Delta t/2$ along x every half-step. The precision of the heat transport in the process zone requires a sufficient number of pixels in the process zone size. A linear size $\Delta x = l/10$ is in practice sufficient - it has shown on examples to achieve results 3% close to those obtained with $\Delta x = l/20$ and $\Delta x = l/40$. A similar precision is achieved with a choice of time steps equal to $\Delta t = 0.9(\Delta x)^2/D$ or smaller.

This leads to the following system to obtain the temperature field after the first half iteration: using the notation $s = D\Delta t/[2(\Delta x)^2]$,

$$\begin{aligned}
(1+2s)u^{n+1/2}_{i,j} - su^{n+1/2}_{i-1,j} - su^{n+1/2}_{i+1,j} = \qquad (11)\\
(1-2s-1/\tau)u^n_{i,j} + su^n_{i,j-1} + su^n_{i,j+1} + \frac{\Delta t}{2}\Omega^n_{i,j}
\end{aligned}$$

In matrix form, this is written for every column $j \in \{1, N_y\}$ as

$$\begin{pmatrix} (1+2s) & -s & 0 & \cdots & 0 \\ -s & (1+2s) & -s & \ddots & 0 \\ 0 & \ddots & \ddots & \ddots & \vdots \\ \vdots & & \ddots & \ddots & -s \\ 0 & \cdots & 0 & -s & (1+2s) \end{pmatrix} \begin{pmatrix} u_{1,j}^{n+1/2} \\ u_{2,j}^{n+1/2} \\ \vdots \\ \vdots \\ u_{N_x,j}^{n+1/2} \end{pmatrix} = \begin{pmatrix} (1-2s-1/\tau)u_{1,j}^n + su_{1,j-1}^n + su_{1,j+1}^n \\ (1-2s-1/\tau)u_{2,j}^n + su_{2,j-1}^n + su_{2,j+1}^n \\ \vdots \\ \vdots \\ (1-2s-1/\tau)u_{N_x,j}^n + su_{N_x,j-1}^n + su_{N_x,j+1}^n \end{pmatrix} + \frac{\Delta t}{2} \begin{pmatrix} \Omega_{1,j}^n \\ \Omega_{2,j}^n \\ \vdots \\ \vdots \\ \Omega_{N,j}^n \end{pmatrix} \quad (12)$$

where the boundary conditions $u_{i,j} = 0$ are used in the second hand term when $i = -1, j = -1, i = N_y + 1$ or $j = N_x + 1$. The inversion of this tridiagonal matrix is done for every j using the TDMA algorithm[2].

The second half-step is done with the same logic, for every $i \in \{1, N_x\}$, by inversion of the following tridiagonal system:

$$\begin{pmatrix} (1+2s) & -s & 0 & \cdots & 0 \\ -s & (1+2s) & -s & \ddots & 0 \\ 0 & \ddots & \ddots & \ddots & \vdots \\ \vdots & & \ddots & \ddots & -s \\ 0 & \cdots & 0 & -s & (1+2s) \end{pmatrix} \begin{pmatrix} u_{i,1}^{n+1} \\ u_{i,2}^{n+1} \\ \vdots \\ \vdots \\ u_{i,N_y}^{n+1} \end{pmatrix} = \begin{pmatrix} (1-2s-1/\tau)u_{1,j}^{n+1/2} + su_{1,j-1}^{n+1/2} + su_{1,j+1}^{n+1/2} \\ (1-2s-1/\tau)u_{2,j}^{n+1/2} + su_{2,j-1}^{n+1/2} + su_{2,j+1}^{n+1/2} \\ \vdots \\ \vdots \\ (1-2s-1/\tau)u_{N_x,j}^{n+1/2} + su_{N_x,j-1}^{n+1/2} + su_{N_x,j+1}^{n+1/2} \end{pmatrix} + \frac{\Delta t}{2} \begin{pmatrix} \Omega_{i,1}^{n+1/2} \\ \Omega_{i,2}^{n+1/2} \\ \vdots \\ \vdots \\ \Omega_{i,N_y}^{n+1/2} \end{pmatrix} \quad (13)$$

There are thus N_x inversions of tridiagonal matrices of size $N_y \cdot N_y$ and N_y inversions of tridiagonal matrices of size $N_x \cdot N_x$ per full time step - the algorithm requires $O(N)$ operations, where $N = N_x \cdot N_y$ is the number of knots, and is of second order in space and time, i.e. its precision if of order $O(\Delta t^2)$ and $O(\Delta x^2)$.

5 Joint instantaneous evaluation of energy release rate and Joule power.

To illstrate the variability of the system from an experiment to another, and through time during one experiment, we present here another detailed analysis of the main observables, usig another experimental example carried out under conditions identical to the one presented in the main text. Snapshots of the experimentally measured temperature are displayed on Fig. 13. A fast propagation stage, associated to a large temperature increase, happens transiently and is shown on Fig. 13(b). Determining the velocity of the hottest spot, shown on Fig. 14 (a), the crack tip is also seen to oscillate between a slow regime, with a propagation around $1mm/s$, and a fast one with a velocity $v > 1cm/s$. Contrarily to the case in the main text, the stage at high velocity happens far from the external boundary, and only lasts for a small portion of the crack trajectory - it is followed by a slow motion stage for the rest of the experiment. In this experiment, the instantaneous tracking of force and boundary displacement allows to determine instantaneously the force $F(t)$ and displacement $\delta(t)$. It was checked that the elastic behavior of the paper sheet is close to linear, i.e. it presents an instantaneous relation during unloading of the type $F = k(\delta - \delta_0)$, where δ_0, the undeformed elongation, is close to a constant during the process, and k is a constant (during the unloading - it changes when the crack progresses). Hence, the elastic energy can be estimated as

$$E_{el}(\delta) = \int_{\delta_0}^{\delta} F(\delta)d\delta = (1/2)k(\delta - \delta_0)^2 = (1/2)F(\delta)(\delta - \delta_0). \quad (14)$$

The change in elastic energy during crack propagation is thus

$$dE_{el} = (1/2)d[F(\delta)(\delta - \delta_0)]. \quad (15)$$

This can also be evaluated as $dE_{el} = (1/2)d(k(\delta-\delta_0)^2) = k(\delta - \delta_0)d\delta + (1/2)(\delta - \delta_0)^2 dk = F(\delta)d\delta + E_{el}dk/k = dW + E_{el}dk/k$, The work brought by the external mechanical setup on the paper, is

$$dW = Fd\delta. \quad (16)$$

The total change in mechanical energy, in the loading setup plus the paper, corresponds to[3]

$$dE_m = dE_{ext} + dE_{el} = -dW + dE_{el} = E_{el}dk/k. \quad (17)$$

To obtain this instantaneous change, dW, dE_{el} and dE_m are evaluated via the above expressions Eqs. (15,16,17) from the experimentally measured series of elongation $\delta(t)$ and force $F(t)$ and from $\delta_0 = \delta(t_0)$, the initial elongation. These expressions and their relationship to the displacement-force relation are illustrated on Fig. 12.

The instantaneous rate $-dE_m/dt$, evaluated over 1 s long time intervals, is shown on Fig. 14 (b).

The energy release rate is by definition the ratio between the mechanical energy change $-dE_m$ and the surface created $dS =$

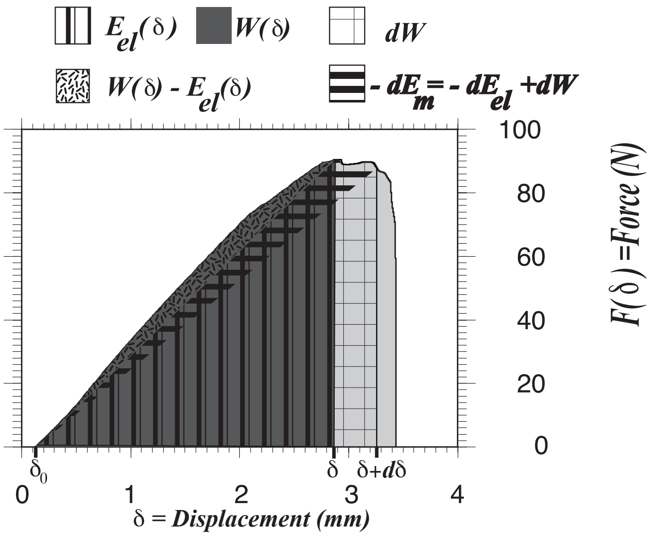

Fig. 12 Incremental variations of work, elastically stored energy, and total mechanical energy during an experiment, from the force displacement curve.

$hvdt$: Thus, Fig. 14 (b). corresponds to $-dE_m/dt = GdS/dt$, and the ratio $G = -(dE_m/dt)/(hv)$ is shown on Fig. 14 (c), when the two quantities in the ratio are not too small - to avoid too large errors.

The power of the heat release is determined by integration of the temperature excess along a transverse profile 0.5 mm behind the crack tip (hottest point), leading to $I_0(t)$. The heating power corresponding, $I_0(t)/(\rho c)$, is shown on Fig. 14 (d). The total ratio of these powers, Joule heating rate over mechanical energy release rate, $\alpha_T = I_0(t)/(\rho c G)$, fluctuates for most of the experiment, and jumps to a significantly higher value after the crack jumps to a high velocity. There are nonetheless important fluctuations in this instantaneous estimate, which can be attributed to the imprecision of the instantaneous energy estimates - ratios of small numbers give artifacts of jumps to high values of α. Typically, measured low values of G give an apparent high value of α. Independently from this tendency, we not a jump to a higher value of α when the crack jumps at velocities exceeding $1cm/s$. The fact that velocity jumps correlate reasonably with an increase of α is compatible with the triggering during this velocity jumps, of a mechanism where a fraction of the energy coming from an exothermal reaction. Note that this jump to high velocities is significantly away from the boundaries (around 4 cm away in a sample of 10 cm by 10 cm), so that this increase of α, in this experiment, cannot be attributed to different interactions with the boundaries. Such a case is analysed in Figs. 14 and 13.

References

1 Butkov, E., Mathematical Physics, Addison-Wesley. (1968)

2 Press, W.H. et al., Numerical Recipes in Fortran 77: The Art of Scientific Computing, Cambridge University Press, 2nd ed. (1992).

3 Lawn, B., Fracture of brittle solids, Cambridge University Press, 2nd ed. (1993).

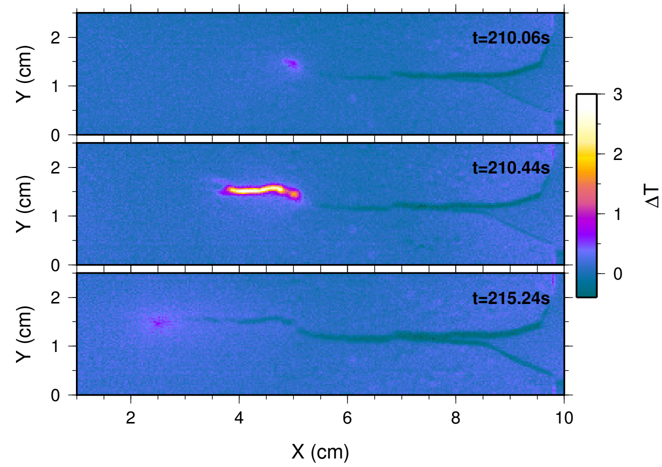

Fig. 13 Experimentally measured temperature rise, in Kelvins, during the experiment analysed in Fig. 14. The event at large velocity (middle plot) is transient and, in this case, happens far from the boundaries.

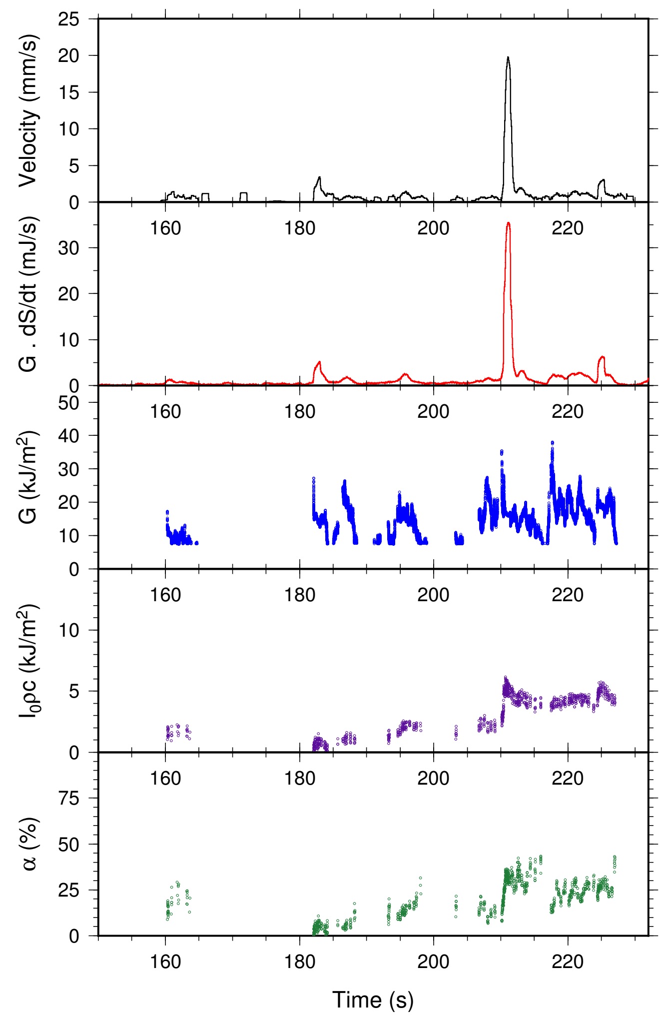

Fig. 14 Experimental determination of (a) velocity v of the hottest point, (b) total mechanical power brought to the system $-dE_m/dt = -dW/dt + dE_{el}/dt$. (c) Energy release rate $G = -(dE_m/dt)/(hv)$. (d) Heat release rate determined from transverse temperature profiles $I_0(t)/\rho c$. (e) Heating ratio $\alpha_T = I_0(t)/(\rho c G)$.